



Validation of a Transonic Lattice-Boltzmann Method on the NASA Common Research Model

Benedikt König*, and Ehab Fares†

Exa GmbH, Curiestrasse 4, Stuttgart, 70563, Germany

A novel transonic Lattice-Boltzmann Method is validated against the NASA Common Research Model. This model offers the most comprehensive experimental data base available but also suffers from a number of issues that make a comparison to CFD difficult. In order to achieve a rigorous validation of the new code, the major effects present in the wind tunnel experiments are included in the modeling. This work describes Lattice-Boltzmann simulations of the Common Research Model with updated wing twist distributions and including the wind tunnel support system. Preliminary results for both the baseline geometry and the updated model are presented and show a promising correlation to the experiments.

I. Introduction

In the *CFD Vision 2030 Study*,¹ an advisory team to NASA analyzed the current state of CFD and its future potential and challenges. One of the conclusions was that CFD is nowadays very successfully applied but that, at the same time, its reliable use is limited to certain areas. The reason for that was seen in the inability to accurately and reliably predict turbulent separated flows. And the current CFD workhorses based on the Reynolds-averaged Navier-Stokes (RANS) equations are considered unlikely to overcome this. One could argue that those methods have peaked out in their development and a paradigm change is necessary to move forward in the future.

The Lattice-Boltzmann method (LBM) on the other hand, is a relatively new technology. It has evolved over the last years into a viable alternative to the classical CFD methods, which are mostly based on RANS. The *CFD Vision 2030 Study*¹ explicitly names it as one of the “novel nontraditional approaches” that should be investigated for the future. LBM has recently been validated for a number of aerospace-related applications and, more importantly, it has also been used for a number of applications where it went beyond what was previously possible with CFD.²⁻⁴ But despite those successes and the potential to overcome some of the major deficits RANS tools face, there has been one significant limitation for LBM up until recently. The standard LBM scheme, as it was also employed in the commercial LBM solver PowerFLOW®, is restricted to subsonic Mach numbers. This restriction limits the range of applications for standard LBM within the aerospace field. While some effort were made to extend the range of Mach numbers for LBM, no such tool was available for industrially relevant cases. Only recently, a first validation of an extended LBM scheme in the PowerFLOW code was published by Fares et al.⁵ that opened up the range of flow velocities from purely subsonic up to supersonic Mach numbers. As a further step in the validation process, a similar method is now applied to and validated on a transonic aircraft configuration.

Of the limited number of publicly available transonic aircraft models, the NASA Common Research Model^{6,7} (NASA-CRM) offers the most comprehensive experimental database for CFD validation. The CRM was first introduced at the fourth AIAA Drag Prediction Workshop⁸ (DPW) and later considered again in the fifth DPW.⁹ At these two workshops it became clear that the model and its experimental results pose some significant challenges, even to current state-of-the-art CFD methods. Hence, in order to use this model for validation of a new CFD method, a very rigorous comparison is necessary to ensure that the validation is not confounded by non-modeled effects. In a recent work, Rivers¹⁰ investigated the source of the differences found between the experiments on the CRM and the numerical simulations. Two main contributors were

*Senior Application Engineer, Aerospace.

†Technical director, Aerospace, senior AIAA member.

identified, namely a difference in the wing twist distribution between the design shape and the actual wind tunnel model during the tests, and a non-negligible effect of the model support system in the wind tunnel. In order to be able to validate the new transonic LBM solver against those experiments, the two effects are taken into account in the modeling. The results presented here give a snapshot of the current status of this validation. It describes ongoing work, both in terms of the validations, but also with respect to the development of the transonic LBM code.

II. Numerical Method

A Lattice-Boltzmann method is used for the simulation of the flow. For more information about this method the reader is referred to works by Chen et al.¹¹ and Qian et al.¹² For the simulations presented in this work, a newly developed transonic beta version of the LBM method was employed, similar to what was described by Fares et al.⁵ For a more complete coverage of the scientific basics of the new transonic LBM scheme the reader is referred to [13–15].

In order to capture boundary layers for high Reynolds number flows, a wall modeling approach is employed here. The turbulence modeling approach, called LBM-Very Large Eddy Simulation (LBM-VLES), is incorporated in the solver PowerFLOW. This approach is characterized by modeling the impact of turbulence in areas where possible (such as attached boundary layers) and by resolving turbulent fluctuations in areas where necessary (such as flow separations). Lattice-Boltzmann methods are uniquely suitable for performing this type of simulation because they are by definition unsteady and have very low artificial dissipation. For a more detailed description on LBM-VLES the reader is referred to these publications.^{16–21} Additional validation studies performed with PowerFLOW have been published in the past.^{22–26}

III. Model

In this section, the NASA Common Research Model will be briefly described, including an overview of some of the relevant available experimental data and the issues encountered when modeling it in CFD.

III.A. The NASA-CRM

The NASA-CRM offers arguably the most complete publicly available experimental database for a contemporary transonic aircraft configuration. For that reason, it has seen a lot of attention in various international projects, beyond its original use in the Drag Prediction Workshop series. But still, one of its first uses, even before it was actually tested in wind tunnels, was as the test case for the fourth AIAA CFD Drag Prediction Workshop.⁸

Background

The CRM was developed by Vassberg et al.⁶ specifically as a model for CFD validation. It features a modern transonic supercritical wing for a cruise Mach number of $M = 0.85$ at a design lift coefficient of $C_L = 0.5$. While the model was intentionally designed to “exhibit fairly high performance over a reasonable neighborhood of the design point”,⁶ the fact that it uses a supercritical wing will give rise to certain issues discussed further down.

A number of configurations of the CRM were developed right from the start. The first configuration consists of the wing and fuselage only and is typically denoted as WB. Within the DPW series, this WB configuration is typically used for grid convergence studies. The second configuration (WBPN) also includes a flow-through nacelle with pylon installed on the wing. The third configuration with horizontal tail plane, but without nacelle and pylon, (WBT) is the one which will be used in the study presented here.

The original CRM wind tunnel model, but also a number of scaled versions and derived models, have been experimentally tested in various wind tunnels all over the world.^{27–30} In this work, data from the entries into the NASA Langley National Transonic Facility (NTF) and the European Transonic Wind Tunnel (ETW) will be used. Those two wind tunnels can operate under pressurized cryogenic conditions to achieve flight Reynolds numbers.

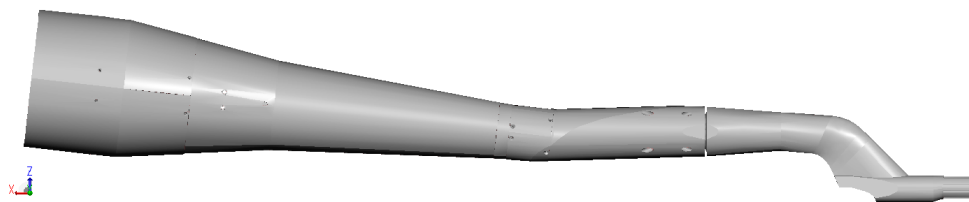


Abbildung 1. Illustration of the CAD model of the ETW blade sting assembly; seals, screws and bolts are not shown here (model courtesy of M. Wright, ETW)

Experimental Results

The experimental data used in this validation work is publicly available from the respective repositories for the NASA wind tunnel tests⁷ and for the European ESWIRP project.³¹ An initial comparison of the classical wind tunnel measurements (i. e. forces, moments and wall pressures) was presented in [28]. The experimental results for forces, moments and wall pressures used in this work are Test 197, Run 92 for the NTF data and Run 153 of the ESWIRP campaign in ETW. Aeroelastic deformations from ETW are given in Run 182.

In both wind tunnels, the CRM model was mounted using a blade sting support system which attaches to the model in place of a vertical tail plane. The front part of that sting, the blade, was identical in both tunnels, but further downstream the actual sting supports differed. A CAD model of the sting used at ETW is shown in Figure 1. According to Rivers,²⁸ the NTF experimental data has not been corrected for effects of this mounting system. The data from ETW on the other hand is provided with three different correction standards. The first set of data has a similar level of corrections as the one from NTF, i. e. wall interference corrections have been applied to forces and moments, but no sting support corrections. This is the dataset used for comparisons in this work. Alternatively, a second set (FF corrected) is provided including also a correction for sting buoyancy, the effect of the pressure gradient created by the sting on the cross sectional area distribution of the model (M. Wright, ETW, personal communication, June 2015). This second dataset would be best suited for comparison to free flight CFD simulations. It will not be used in this study, however, as the sting buoyancy correction is not able to correct the effect of the sting on the wing pressure distribution. A third dataset (no WIC) is made available which contains no sting corrections and no wall interference corrections on model loads and pressures. This dataset would be appropriate to compare to for simulations including the wind tunnel test section. Simulation of the wind tunnels walls is considered to be not necessary, however, as the slotted-wall concept employed in tunnels like NTF and ETW typically helps to reduce wall interference effects to a minimum. Also, modeling a complete slotted-wall test section in CFD is a very challenging task, way beyond this validation exercise.

A comparison of the results for the forces and the pitching moment from NTF and ETW is shown in Figure 2 for $M = 0.85$ and $Re = 5 \times 10^6$. It is interesting to note that both wind tunnels agree very well on lift when wall interference corrections are included. For drag, the buoyancy correction applied at ETW leads to a significant increase which shows that the pressure gradient induced by the sting support system is not negligible. The pitching moment shows a pronounced pitch break in all datasets just above $\alpha = 3^\circ$ that correlates to the onset of the non-linear range in the lift curve.

Drag Prediction Workshop Results

The NASA-CRM was first introduced as a blind test for the fourth AIAA CFD Drag Prediction Workshop.⁸ CFD flow solutions for 16 different conventional RANS-based flow solvers were submitted. An overview of the lift obtained by those solvers is given in Figure 3. The comparison to experimental results from NTF and ETW shows that all CFD solutions consistently over-predict lift in the order of 10 lift counts. Also indicated is a representation of the spread of all the solutions except for some of the outliers. This approximate bandwidth will be used in the remainder of this work to represent the DPW results in general.

A comparison of the schematic representation of the DPW-4 solutions to the experimental results for lift, drag and pitching moment is given in Figure 4. Here, and consequently in all other plots of forces and moments in this work, a representation of C_D and C_M versus the angle of attack α is chosen, rather than the more customary plot versus the lift coefficient C_L . This is done on purpose to better illustrate the fundamental mismatch between the lift predicted by CFD and the wind tunnel measurements.

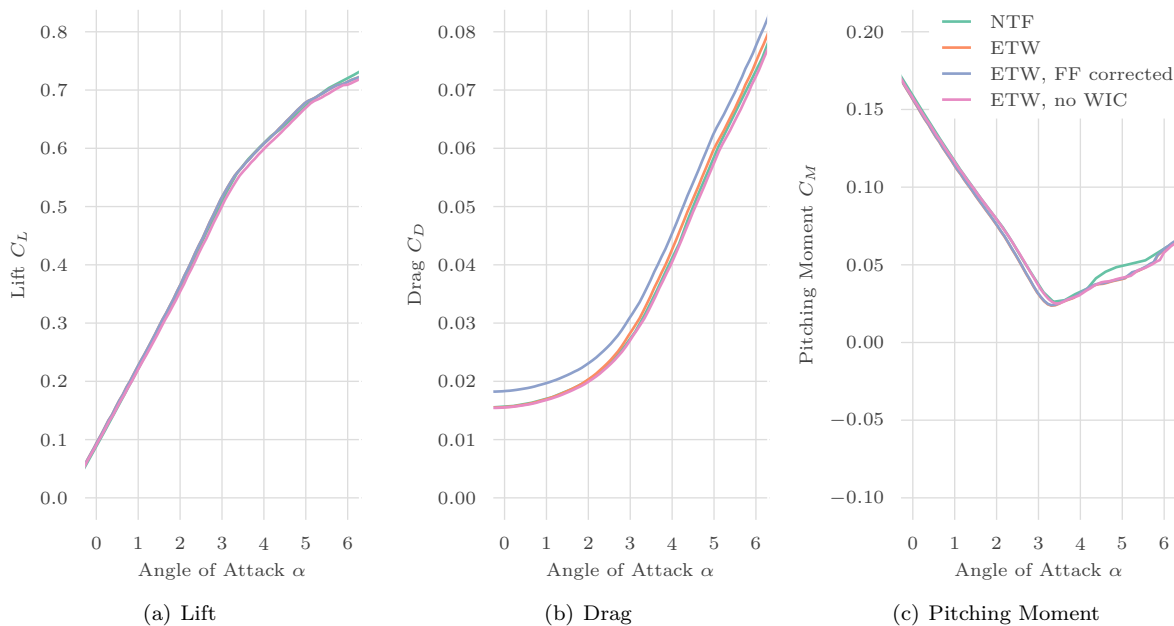


Abbildung 2. Comparison of model loads on CRM at $M = 0.85$, $Re = 5 \times 10^6$ from NTF⁷ and ETW.³¹ ETW data presented with three different correction standards.

The comparison reveals that there were some systematic discrepancies between the CFD modeling and the wind tunnel. It is clear that those differences make the original intention, to use the CRM as a validation vehicle for numerical simulations methods, very difficult. To really be able to validate any CFD result against the experimental CRM data requires to first understand and solve the mismatch between the models.

One known major difference between the wind tunnel setup and the DPW simulation is the presence of the sting support in the former. A large structure like this mounting system will obviously have a noticeable effect even on the far-field flow around the model. From other wind tunnel test campaigns it is, however, not to be expected that the presence of the sting support should have such a considerable impact on the results. Instead, considering the comparison of pressure distributions at various spanwise stations suggests that the effective local angle of attack of the wing is changing in spanwise direction towards the tip.

III.B. Wing Twist Correction

As was discussed further above, the CRM was designed with a supercritical wing. For such a wing, each section of it only delivers its intended performance over a relatively narrow range of Mach numbers and lift

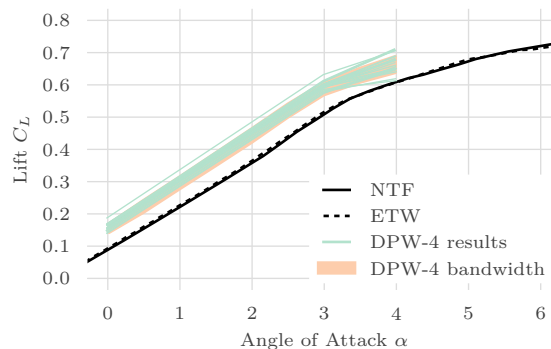


Abbildung 3. Overview of DPW-4 lift results in comparison to NTF and ETW experimental data. The DPW-4 bandwidth approximates the range of all solutions except for some of the outliers (DPW-4 results data taken from [8], bandwidth representation from [10]).

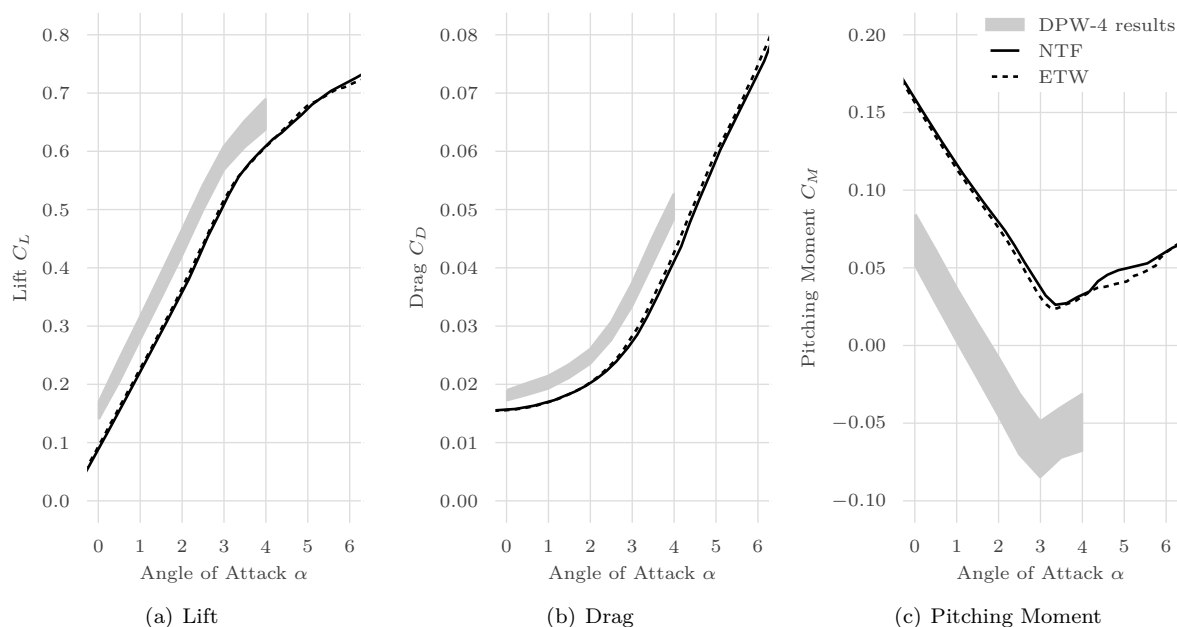


Abbildung 4. Comparison of the DPW-4 results representations for lift, drag and pitching moment to experimental results from NTF and ETW.

coefficients. This makes such airfoils much less robust to changes in incidence than conventional airfoils or airfoils at subsonic conditions in general. Hence, any misprediction of the local angles of attack on the wing will lead to a noticeable deterioration in performance.

It was shown by Rivers¹⁰ that there is actually a mismatch between the wind tunnel model and the one used for CFD simulations. The wind tunnel model of the CRM was in fact built to the design-shape, rather than the so called wind-off shape. The latter would have allowed for the model to deform in the wind tunnel at the design conditions into the design-shape. Those aeroelastic deformations are significant because of the high model-loads achieved under pressurized conditions, as they are typically used for high-Reynolds number wind tunnel testing. Without taking those deformations into account during the build process of the wind tunnel model, the model will take on a different shape than intended. Under loads, the wing twists off towards the tip compared to the wind-off shape. Hence, the CRM geometry in its design shape, as it was provided for the drag prediction workshop series, differs significantly from the shape that was actually tested in the experiments. The sensitive supercritical wing sections on the outboard wing therefore see a reduced local angle of attack.

In order to compensate for this difference in numerical simulations, the aeroelastic deformations have to be

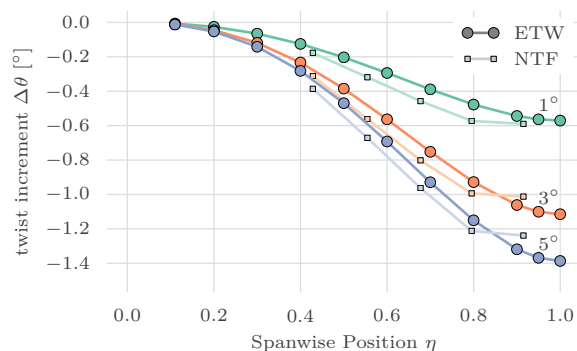


Abbildung 5. Twist increments for wind-on wing shape relative to the baseline (wind-off) wing as measured in the experiments.

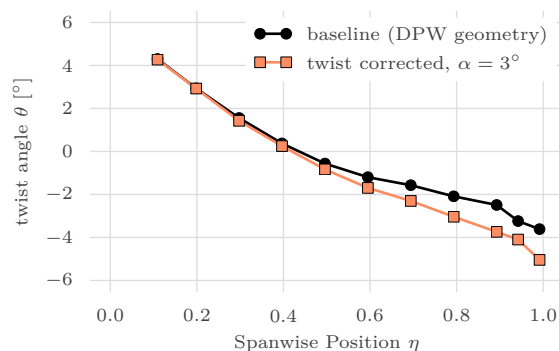


Abbildung 6. Twist distribution for baseline wing and for modified geometry at $\alpha = 3^\circ$, based on twist increment measured in ETW.

applied to the geometry. Those deformations were measured during the test entries at both the NTF and the ETW facilities and the data are available from the respective repositories.^{7,31} Figure 5 shows the increments of the wing twist for a number of angles of attack relative to the design shape, as they were measured during the tests at both NTF and ETW. Tip deflections in the order of $\Delta\theta \approx -1^\circ$ were encountered around at an angle of attack of 3° , close to the design lift coefficient. For supercritical airfoil sections, as they are used on the CRM outboard wing, this results in a considerable difference compared to the design intent.

One way to account for those aeroelastic deflections in CFD is to perform a coupled fluid-structure interaction simulation. Results using this methodology were recently presented by Keye and Rudnik.³² In this case of the CRM experiments, however, deformation data was measured and is available covering a large part of the angle of attack range tested. It is therefore possible to apply the measured shape changes to the baseline geometry and, thus, recover the shape as tested for that particular flow condition. This approach was previously used for the CRM by, for example, Rivers¹⁰ and Eberhardt et al..³³

In this work, the CRM's wing twist distribution is modified based on the experimentally measured twist increments. For the initial results presented here, only the wing twist is considered and wing bending as well as the stabilizer deformations are neglected. Those are expected to have minor effects only. The geometry deformation was done based on the baseline geometry using the PowerDELTA[®] geometry processing software by Exa. In PowerDELTA, curvature continuous geometry morphing is done using a lattice with an arbitrary number of control points. In this case, the lattice was fit around the CRM baseline wing and a total of 11 stations were defined, corresponding to the 11 spanwise positions where deformation measurements of the wing were taken during the ETW tests. An illustration of the undeformed lattice is given in Figure 7(a). For each of the 11 spanwise sections, a rotation was defined around the spanwise axis through the quarter chord point at that position. Second order interpolation was applied between the sections. The resulting morphed geometry (with enlarged deformations for visualization purposes) is depicted in Figure 7(b). A spanwise twist distribution for an angle of attack of $\alpha = 3^\circ$ is compared to the baseline twist distribution in Figure 6.

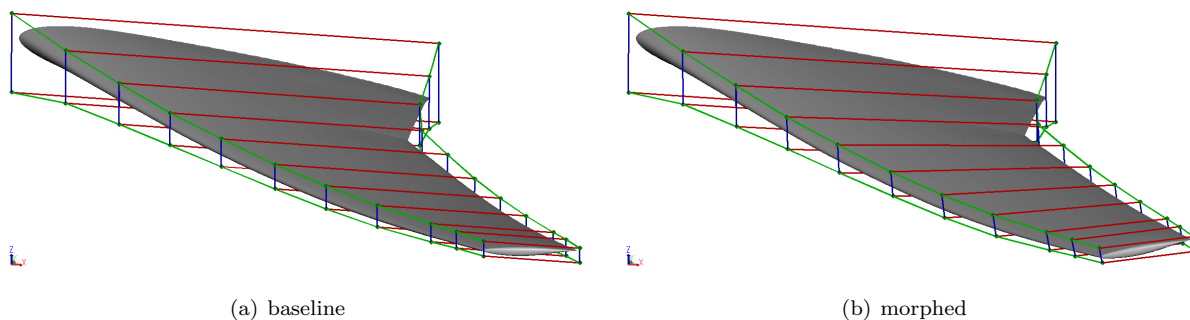


Abbildung 7. The morphing lattice on the baseline wing (a) and on the morphed geometry (b).

III.C. Simulation Setup

The PowerFLOW simulations presented in this work were performed on the so-called WBT0 model of the NASA-CRM, i. e. on the wing/body configuration with horizontal tail plane at 0° setting angle. This is the same configuration that was used for the fourth and fifth drag prediction workshops. Besides the baseline geometry as it was used in DPW-4 and -5, additional variants were simulated including the sting support and with different twist distributions applied to the wing. An illustration of the CFD model with sting support is shown in Figure 8. The sting model from Figure 1 was here extended by an approximate representation of the sting boss as it is present in ETW.

All simulations were conducted using far-field boundary conditions on a box-shaped flow domain in a distance of $50 \times$ (half span) from the half-model. A static pressure outlet condition was applied at the downstream boundary and a velocity boundary condition everywhere else. The resulting Cartesian volume grid, coarsened for visualization, is depicted in Figure 9. An illustration of the locations of the pressure sections as they will be used in this work is shown in Figure 10.

The unsteady simulations of the WBT0 configuration without sting support, when started from scratch, typically had an initial transient time in the order of around three flow passes based on the fuselage length. For the simulations with sting, however, this initial transient time was significantly longer than 20 flow passes,

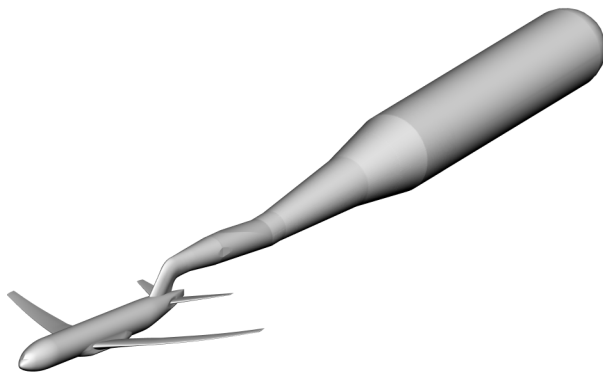


Abbildung 8. The NASA-CRM geometry including blade sting support system.

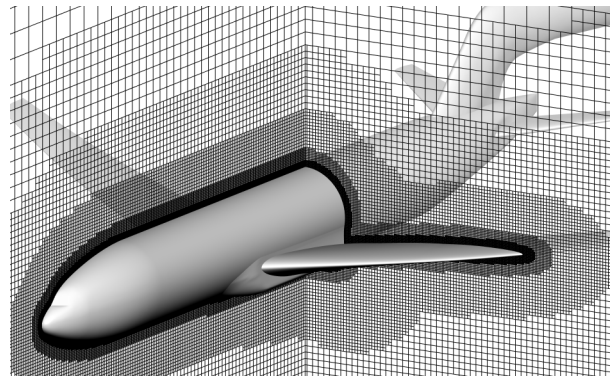


Abbildung 9. The Cartesian grid around the NASA-CRM (grid coarsend for illustration purposes).

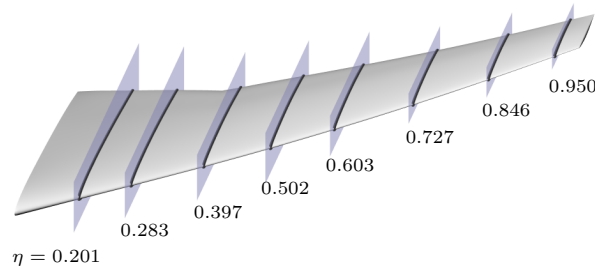


Abbildung 10. Locations of the pressure sections presented in this work.

due to the much larger dimensions of the support. It was therefore not economical to start each simulation from scratch. Here, a scheme was devised starting each simulation on a coarser grid derived from the final one. On that coarsened grid the far-field induction effect of the sting support was converged at a reduced computational effort before using that coarse solution to initialize the final simulations.

IV. Results

IV.A. Grid Convergence Study

A grid convergence study was conducted on the WBT0 baseline configuration at $M = 0.85$, $\alpha = 2.9^\circ$, and $Re = 5 \times 10^6$. Three grid resolution levels *coarse*, *medium*, and *fine* were simulated, with a ratio of 1.5 for each refinement step. According to the practice used in the drag prediction workshop series, the results are plotted versus $N^{-2/3}$, with N being the total number of grid cells. Different to the DPW practice, results are here shown for constant angle of attack α . Matching C_L was not done in this study.

Figure 11 shows the grid convergence behavior for lift, drag, and pitching moment. Lift, presented in Figure 11(a), is basically converged at the medium resolution level, with the variation from medium to fine being less than 0.1 lift counts. The total variation over all grid levels is also small, less than 0.3 lift counts.

Drag on the other hand, as shown in Figure 11(b), exhibits a clear convergence trend but with a large variation with grid resolution. From coarse to fine, drag is decreasing by almost 40 drag counts. It is, however, promising to see that drag is clearly converging. From Figure 4(b) it can be deduced that the classical RANS tools used at DPW-4 predict drag in the order of $C_D = 0.033 \dots 0.035$ for their medium resolution. Applying Richardson extrapolating as described in [8] to the drag data shown in Figure 11(b) yields a continuum value of $C_D = 0.0345$, which is almost 30 drag counts less than the medium resolution result and within the DPW-4 results. A similar dependence can be seen for the pitching moment in Figure 11(c). This grid convergence behavior of drag and pitching moment will be investigated further in the future.

IV.B. Wing Twist and Support Sting Effects

As was mentioned before, Rivers¹⁰ showed that the major discrepancies between the CFD results on the DPW baseline configuration and the actual wind tunnel measurements come from only two aspects. Lift is

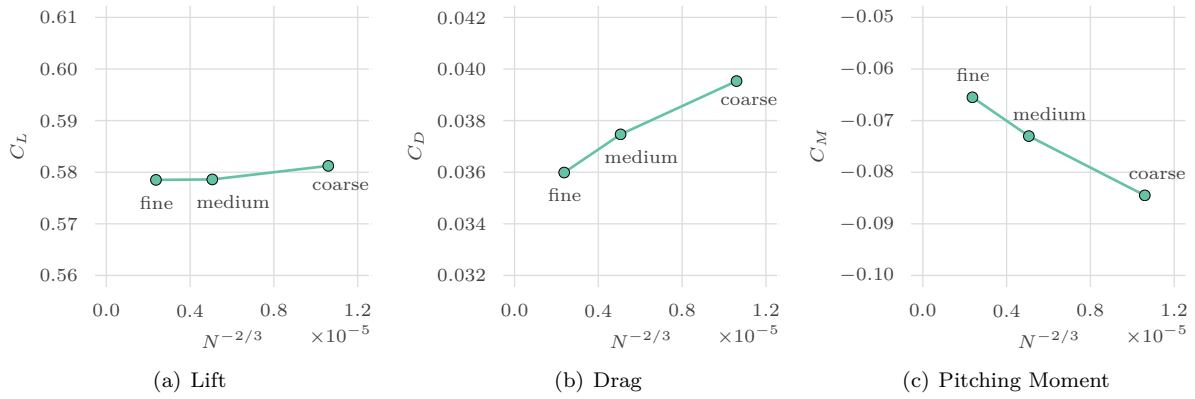


Abbildung 11. Gird convergence behavior of lift, drag and pitching moment.

mostly impacted by the differences in the wing twist distribution due to aeroelastic deformations while drag showed the greatest sensitivity to the modeling of the sting support system.

To reproduce this finding, simulations of three different configurations were conducted for $M = 0.85$, $\alpha = 2.9^\circ$, and $Re = 5 \times 10^6$. The angle of attack of $\alpha = 2.9^\circ$ corresponds to the condition where the design lift coefficient of $C_L = 0.5$ was measured in ETW. Firstly, the baseline geometry WBT0 from the DPW series was used. Secondly, the same geometry was updated according to the method described in subsection III.B with the twist distribution of the main wing measured at ETW for $\alpha = 3^\circ$. The third geometry also included the modified twist distribution but modeled the sting support system too, as shown in Figure 8.

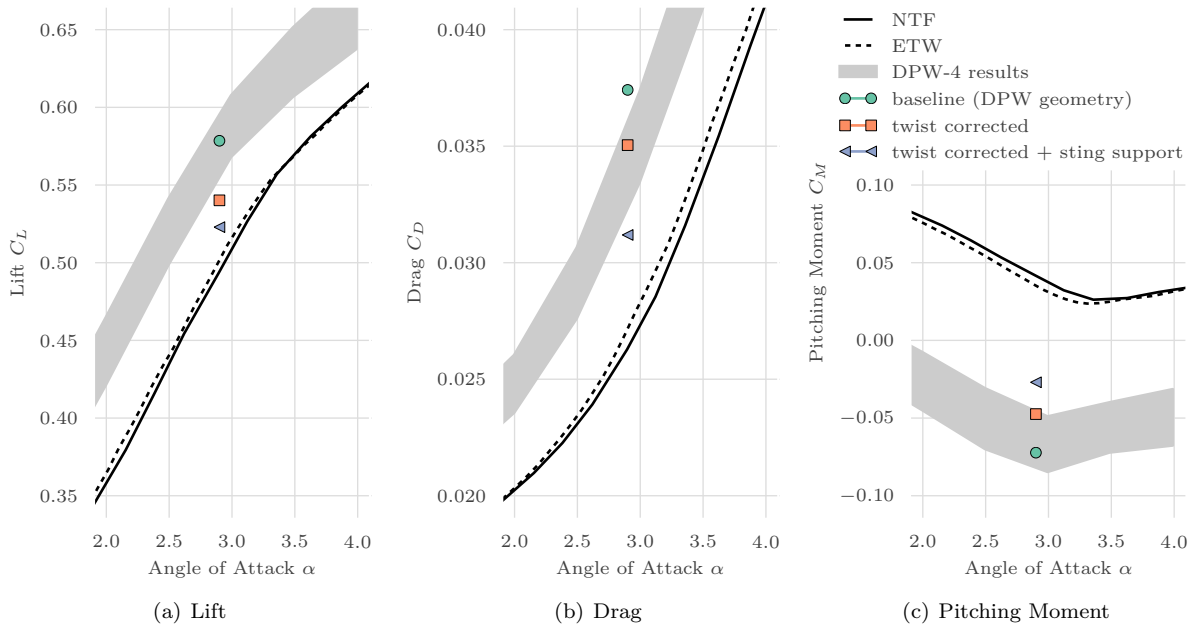


Abbildung 12. Impact of the wing twist distribution and the sting support system on lift, drag and pitching moment. Wing twist distribution as measured in ETW³¹ for $\alpha = 3^\circ$ and with sting support as shown in Figure 8. Results are compared to NTF⁷ and ETW³¹ experimental data.

Force and moment results for the three configurations are presented in Figure 12. They confirm the trends shown by Rivers. The lift coefficient is reduced by almost 4 lift counts or 50% of the initial difference relative to the ETW measurement when the measured twist distribution is taken into account. On top of that, the modeling of the support sting only reduces the difference on lift by an additional 22%. In total, correction of the wing twist and including the support sting in the simulation reduces the initial deviation by 72%.

For the drag coefficient shown in Figure 12(b) the trend is just the opposite. Keeping in mind the strong grid resolution dependence of drag as it was shown earlier it seems reasonable to assess the effects based on the Richardson-extrapolated drag value given above. The relative changes will hence be based on the actual drag values reduced by the 30 drag counts mentioned above for the difference from medium grid to continuum. With that, correcting the twist distribution reduces the initial ΔC_D by 33% or 24 drag counts. Adding the sting support to the simulation takes the resulting drag down by another 39 drag counts, which correspond to more than 50% of the initial difference. Overall, including the two effects in the simulation improves the agreement for drag by 86%.

The pitching moment, however, seems to be affected by more than the twist and the sting support effects. While there is a clear improvement of the agreement to experiments, the pitching moment is still considerably more nose-down in the simulations than in the experiments. Here, the remaining deviation is still more than 50% of the initial one.

Considering the impact on the pressure distribution confirms that including twist and support effects improves the agreement to experiments dramatically. Figure 13 shows a comparison of the three configurations to experimental C_p -distributions. It can be seen that for the inboard section at $\eta = 0.201$ the differences between the three simulations and compared to the experiments are small. Here the change in twist relative to the baseline is small, see Figure 5. Also, the pressure gradient effect of the sting support is small around the wind tunnel centerline, where the calibration for the sting is done at ETW. In fact, the shift of the shock location at this inboard position suggests that the free-stream Mach number should be slightly increased for the simulations with sting support to ensure the same flow velocities along the center of the model.

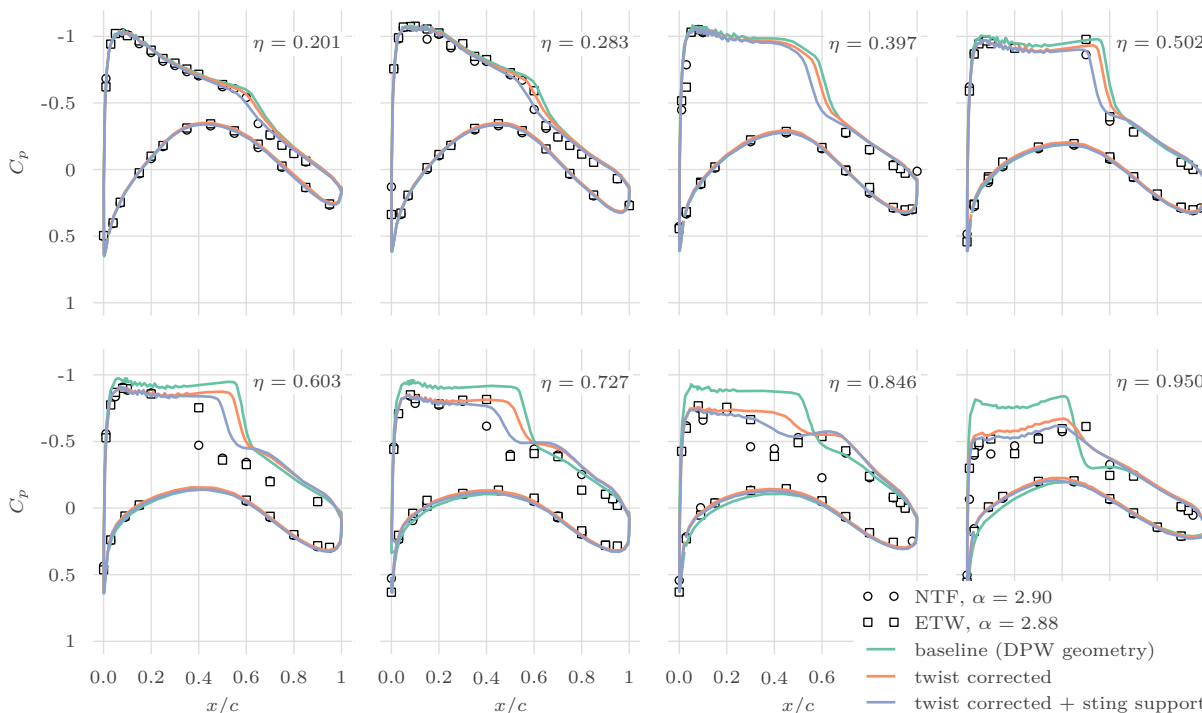


Abbildung 13. Comparison of pressure distributions at $\alpha = 2.9^\circ$ for the baseline geometry and the configurations with corrected wing twist as measured in ETW³¹ for $\alpha = 3^\circ$ and the twist-correction configuration including sting support.

Going further outboard it can be seen how the differences between the three configurations increase. It is interesting to note that the difference in wing twist, going from the baseline to the twist corrected model, shows the clear effect of a reduction of the local angle of attack towards the wing tip. Going outboard, the rooftop level of the pressure distributions gets more and more reduced, which is consistent with lower local angles of attack. The effect of the sting, however, is of a different nature. The suction peaks and rooftop levels are very little affected but the shock position moves more and more upstream. This indicates a local reduction in effective Mach number of the oncoming flow. Comparing the pressure distributions on the outboard wing, i. e. from $\eta = 0.727 \dots 0.95$, one can see that only the inclusion of both the corrected twist and the sting support in the simulations yields a reasonable agreement to experiments.

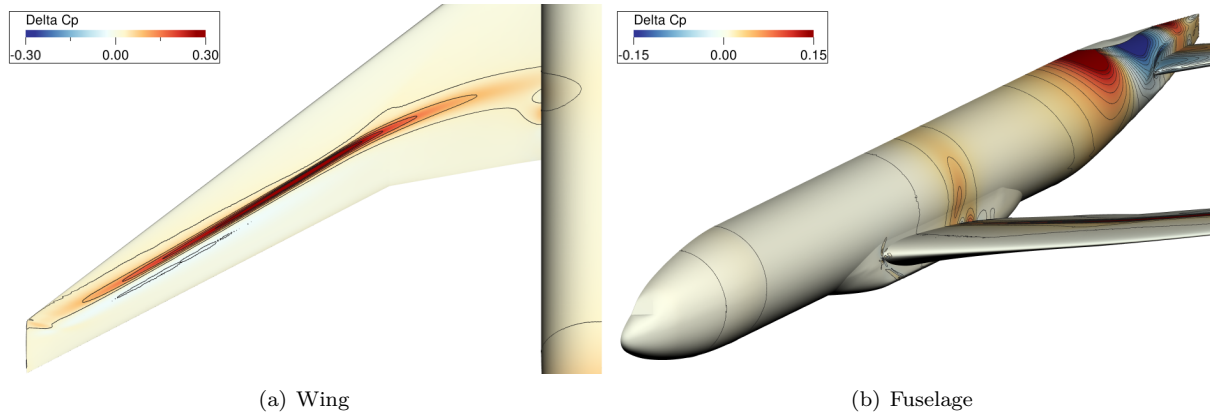


Abbildung 14. Surface distributions of ΔC_p between simulations with and without sting support at $M = 0.85$, $\alpha = 2.9^\circ$, and $Re = 5 \times 10^6$.

The global effect of the sting support on the model can be best seen in a flow visualization, shown in Figure 14. The ΔC_p -distribution on the wing, see Figure 14(a) basically confirms the result seen in the pressure sections in Figure 13. The sting support effect is mostly limited to the position of the shock on the wing. This leads to a reduction in supercritical lift generated in the rooftop region of the pressure distribution. At the same time, the more upstream shock is also slightly weaker, which would probably lead to a reduction in wave drag. On the fuselage, shown in Figure 14(b), the pressure gradient effect in streamwise direction can be seen. Besides some variation of C_p along the fuselage itself there is an distinct overall increase of C_p on the tail cone, leading to a reduction in the fuselage's base drag. Overall, it is clear that including the twist increment and the support system in the simulations is mandatory for a meaningful correlation of the CFD simulations to the experiments.

IV.C. Polar Comparison

Using the baseline configuration and the one including the corrected twist and the sting support, a limited angle of attack sweep was simulated for both. Only results using a fixed twist correction, corresponding to the $\alpha = 3^\circ$ measurement from ETW, for all simulated angles of attack are reported here. The effect of the twist variation for angles of attack other than 3° , which for the range considered here is in the order of $\Delta\theta \approx \pm 0.3^\circ$ compared to the measured tip twist increment of $\Delta\theta = -1.1^\circ$ (see Figure 5), is neglected for now.

Results for forces and pitching moment are presented in Figure 15. For lift, the PowerFLOW results of the baseline simulations agree very well with the results from the DPW-4 but show a nearly constant over-prediction compared to the experimental results. This is in line with the discussion in subsection IV.B. Including both the measured twist and the sting support yields a much better agreement to the measured lift curve, at least within the linear range. The reduction of the lift curve slope between $\alpha = 3^\circ$ and 4° , which is caused by the occurrence of shock induced separations on the wing, seems better captured by the simulation of the baseline shape. A similar trend can be seen in the results presented by Rivers.¹⁰

The drag curve in Figure 15(b) also shows the improved agreement of the simulations including the corrected twist and the sting support. The apparent difference in slope between the baseline PowerFLOW simulations and the DPW-4 results is caused by the strong dependence of drag on the grid resolution, as it was discussed above in subsection IV.A. In fact, the PowerFLOW solution matches the slope of the measured drag curve quite well, only at a higher absolute drag level. Taking into account the $\Delta C_D \approx 30$ drag counts, which were derived as the approximate grid dependent contribution in subsection IV.A, the agreement of the drag curve of the corrected model with the experiments very good.

Similar to the lift curve, the pitching moment in Figure 15(c) shows an improvement in the linear range for the corrected model. However, the non-linear pitch break is reproduced less accurate than in the baseline configuration. Also, as it was shown before in subsection IV.B, the inclusion of the corrected twist and of the sting support in the simulations is not sufficient to fully explain the differences to the experiments. Here, further investigations are necessary.

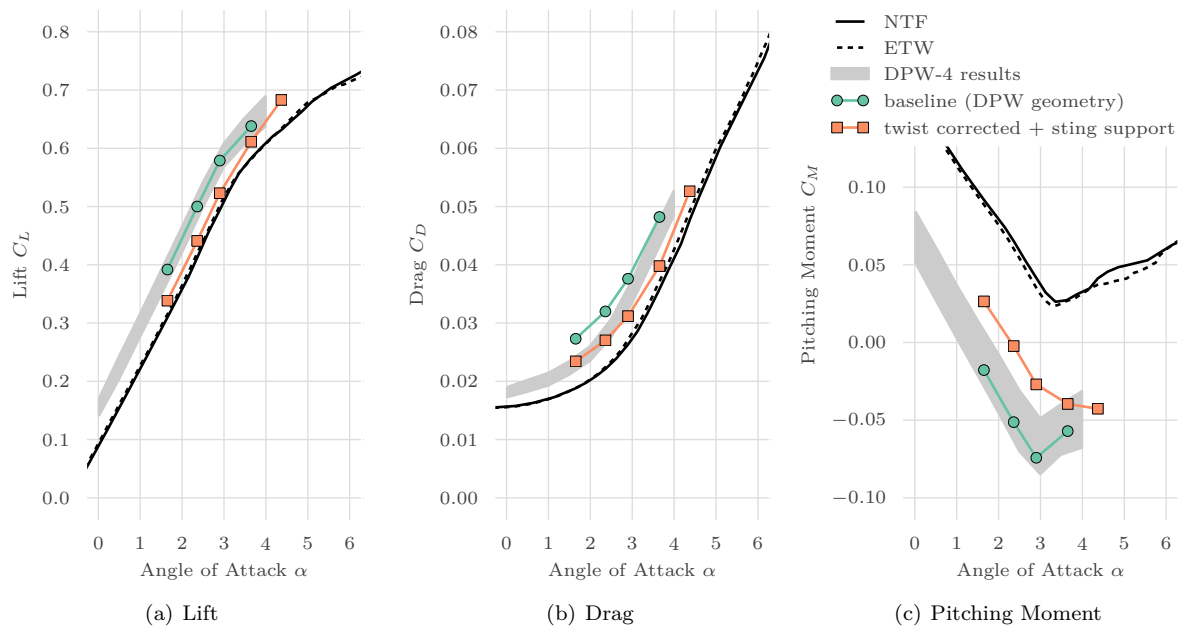


Abbildung 15. Lift, drag and pitching moment comparison for the baseline geometry and the configuration with twist correction (as measured in ETW³¹ for $\alpha = 3^\circ$) and with sting support. Results are compared to NTF⁷ and ETW³¹ experimental data as well as the range of CFD solutions presented to the DPW-4 (data taken from [10]).

To understand the behavior of the lift and pitching moment curves, it is interesting to consider the pressure distributions around the pitch break, when the two models begin to show opposite trends. In Figure 13 the pressure distributions for $\alpha = 2.9^\circ$, just before the pitch break, were already shown. Those can be compared to $\alpha = 3.65^\circ$, given in Figure 16, which is after the pitch break. Here, one striking difference can be seen in the sections on the midboard wing from $\eta = 0.502 \dots 0.727$. The corrected model for the lower angle of attack leads to an upstream movement of the shock over the whole span compared to the baseline model, which is consistent with both the reduced wing twist and the far-field gradient of the Mach number induced by the sting support. For the higher angle of attack, however, the picture is more complicated. The inboard and outboard sections in Figure 16 show the same trend. But in the midboard region the effect is reversed and here the baseline wing yields a more forward shock position. This is the result of a shock induced flow separation which, through its interaction with the shock itself, leads to an upstream movement of the shock. Comparing the simulation results to the experimental values shows, that this effect is even more pronounced in the wind tunnel.

To illustrate this clearer, a series of pressure distribution for increasing angles of attack, from $\alpha = 2.36^\circ \dots 3.65^\circ$, is highlighted side by side for only one spanwise section in Figure 17. The initial trend of moving the shock upstream when the twist correction and sting are included holds up to $\alpha = 2.9^\circ$. This leads to a reduced nose-down pitching moment locally in that section and at the same time to a local reduction in lift which, on this backwards swept wing, results in even less nose-down moment. In summary, the trend up to $\alpha = 2.9^\circ$ is a reduction in lift and in nose-down pitching moment when the twist correction and the support are modeled. This is what Figure 15(a) and 15(c) show. At $\alpha = 3.65^\circ$, however, a rapid forward movement of the shock is seen for the baseline configuration which is not present in the corrected model. This leads to both the reduction of the lift slope in Figure 15(a) as well as the break in the pitch curve. This behavior can only be explained by the occurrence of flow separation, which is better predicted on the baseline wing. One reason for that might be, that the higher local incidences on the baseline model promote stronger shocks and, hence, trigger shock induced separations earlier.

To visualize this suspected impact on a flow separation in the midboard region of the wing a comparison of surface streamlines at $\alpha = 3.65^\circ$ is presented in Figure 18. It can be clearly seen that, while both solutions feature a similar flow separation, it is the baseline configuration in Figure 18(a) where the separation is more pronounced.

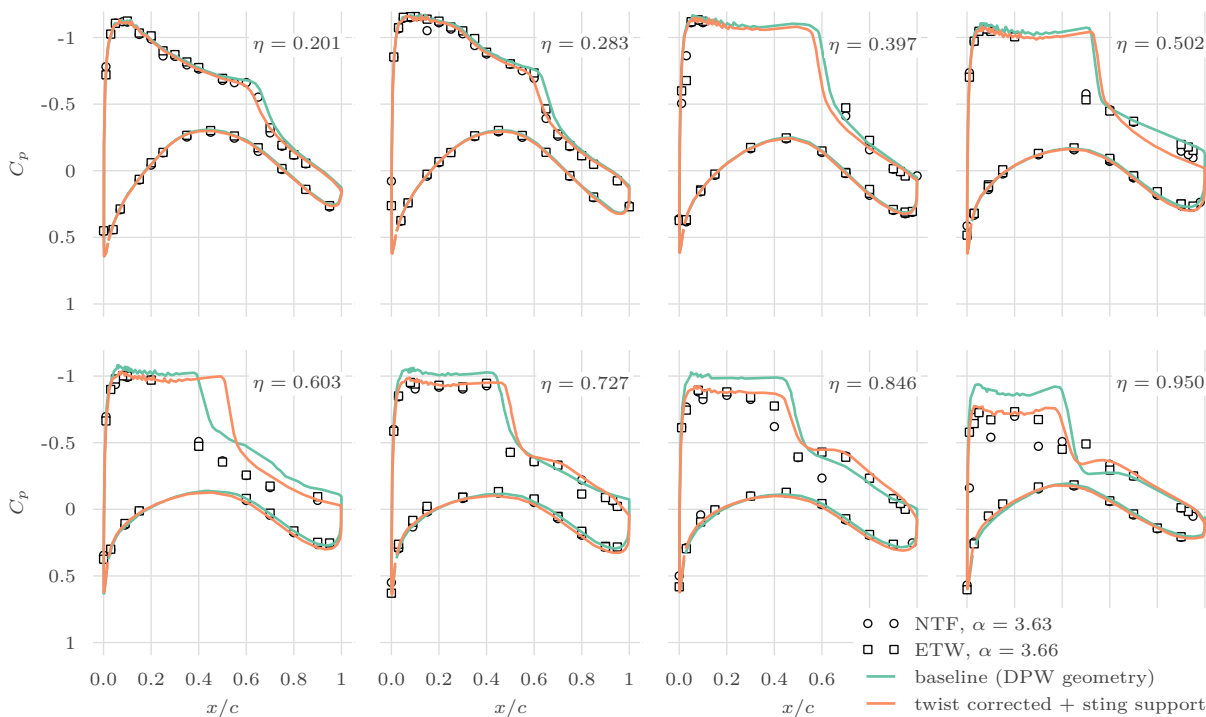


Abbildung 16. Comparison of pressure distributions at $\alpha = 3.65^\circ$ for the baseline geometry and the configuration with twist correction (as measured in ETW³¹ for $\alpha = 3^\circ$) and with sting support.

V. Summary

The current status of the validation work for a novel transonic Lattice-Boltzmann Method on the NASA Common Research Model was presented. An initial assessment of the experimental data and CFD results from the Drag Prediction Workshops is done to highlight the need to include some modifications to the baseline model in order to achieve good agreement. In detail, a correction to the wing twist distribution as measured in the wind tunnel experiments is applied to the CRM model. Also included in the simulations is the wind tunnel support sting for the model. An analysis of the individual effects on the LBM simulation results is presented. Finally, simulations of the baseline model as well as the one including the additional effects are compared to experimental results. It is shown that, while further investigations are still needed, the novel transonic LBM performs well and is able to deliver a good performance prediction of the NASA-CRM.

Besides addressing the issues mentioned in this work, the next steps will extend the simulations into the buffet range. Unsteady simulation results will be compared to the finding reported by Ueno et al.²⁹

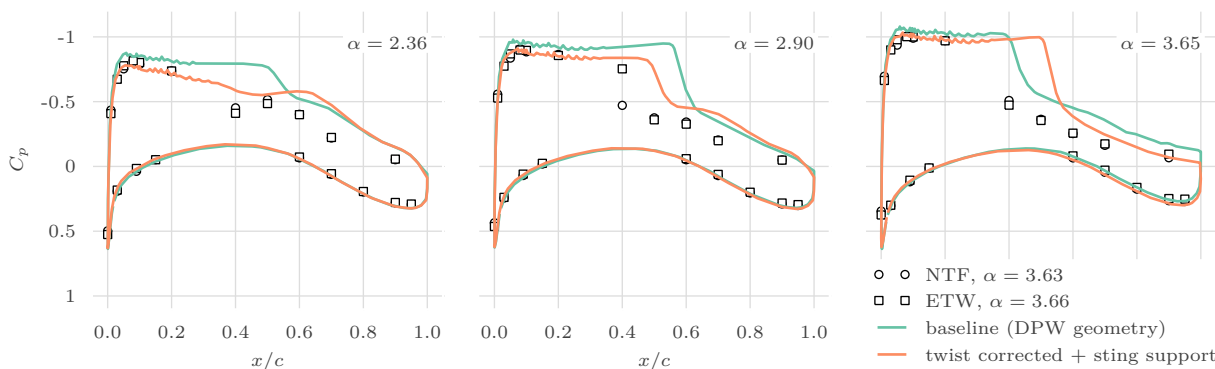


Abbildung 17. Comparison of pressure distributions at $\eta = 60.3\%$ for the baseline geometry and the configuration with twist correction and support sting.

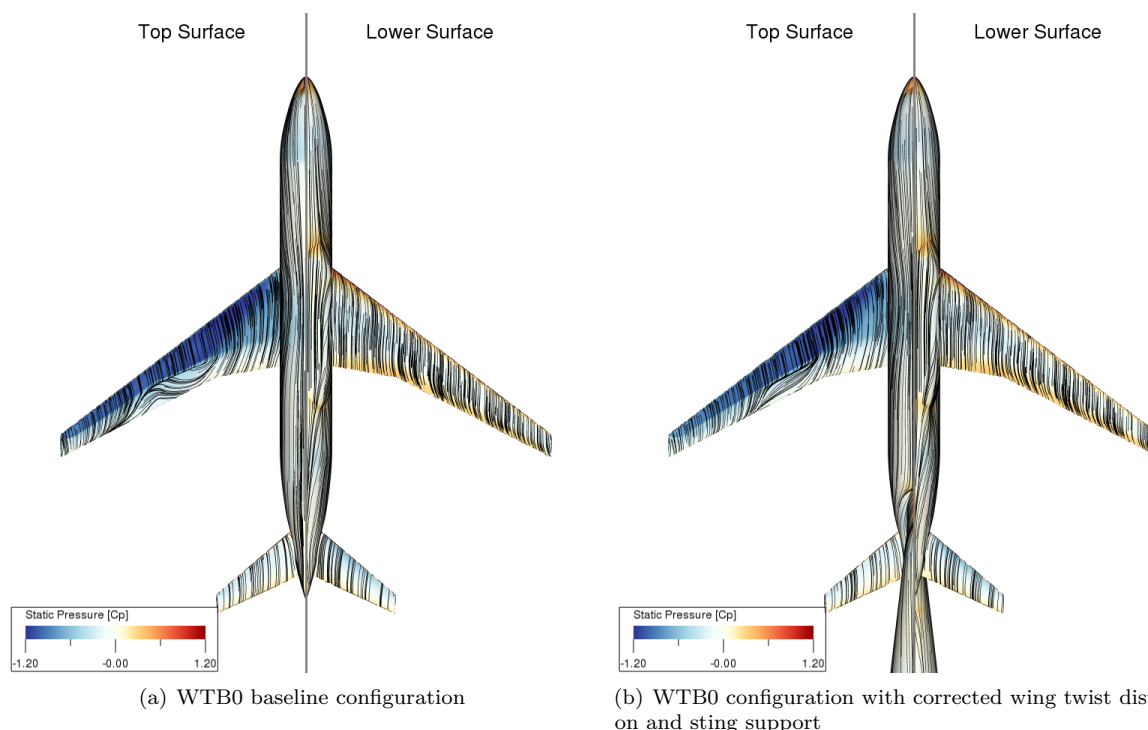


Abbildung 18. Surface streamlines for the baseline geometry and the one with corrected twist and support sting at $\alpha = 3.65^\circ$, $M = 0.85$, and $Re = 5 \times 10^6$.

Acknowledgments

The authors would like to thank Mr. Martin Wright of the European Transonic Windtunnel GmbH (ETW) for providing the sting support geometry and additional explanations about the ESWIRP CRM tests conducted at ETW.

Literatur

- ¹Slotnick, J., Khodadoust, A., Alonso, J., Darmofal, D., Gropp, W., Lurie, E., and Mavriplis, D., "CFD Vision 2030 Study: A Path to Revolutionary Computational Aerosciences," Tech. rep., NASA Langley Research Center, 2014, NASA/CR-2014-218178.
- ²Fares, E., Casalino, D., and Khorrami, M. R., "Evaluation of Airframe Noise Reduction Concepts via Simulations Using a Lattice Boltzmann Approach," *21st AIAA/CEAS Aeroacoustics Conference*, 2015, AIAA 2015-2988.
- ³König, B., Fares, E., and Broeren, A. P., "Lattice-Boltzmann Analysis of Three-Dimensional Ice Shapes on a NACA 23012 Airfoil," SAE Technical Paper 2015-01-2084, 2015.
- ⁴Rougier, T., Bouvy, Q., Casalino, D., Appelbaum, J., and Kleinclaus, C., "Design of quieter landing gears through lattice-Boltzmann CFD simulations," *21st AIAA/CEAS Aeroacoustics Conference*, 2015, AIAA 2015-3259.
- ⁵Fares, E., Wessels, M., Li, Y., Gopalakrishnan, P., Zhang, R., Sun, C., Gopalaswamy, N., Roberts, P., Hoch, J., and Chen, H., "Validation of a Lattice-Boltzmann Approach for Transonic and Supersonic Flow Simulations," *52nd Aerospace Sciences Meeting*, 2014, AIAA 2014-0952.
- ⁶John C. Vassberg, M. A. D., Rivers, S. M., and Wahls, R. A., "Development of a Common Research Model for Applied CFD Validation Studies," *26th AIAA Applied Aerodynamics Conference*, 2008, AIAA 2008-6919.
- ⁷Rivers, M., "NASA Common Research Model," <http://commonresearchmodel.larc.nasa.gov/>, retrived October 12th, 2012.
- ⁸Vassberg, J. C., Tinoco, E. N., Mani, M., Rider, B., Zickuhr, T., Levy, D. W., Brodersen, O. P., Eisfeld, B., Crippa, S., Wahls, R. A., Morrison, J. H., Mavriplis, D. J., and Murayama, M., "Summary of the Fourth AIAA CFD Drag Prediction Workshop," *28th AIAA Applied Aerodynamics Conference*, 2010, AIAA 2010-4547.
- ⁹Levy, D. W., Lafin, K. R., Tinoco, E. N., Vassberg, J. C., Mani, M., Rider, B., Rumsey, C. L., Wahls, R. A., Morrison, J. H., Brodersen, O. P., Crippa, S., Mavriplis, D. J., and Murayama, M., "Summary of Data from the Fifth AIAA CFD Drag Prediction Workshop," *51st AIAA Aerospace Sciences Meeting*, 2013, AIAA 2013-0046.
- ¹⁰Rivers, M. B., Hunter, C. A., and Campbell, R. L., "Further Investigation of the Support System Effects and Wing Twist on the NASA Common Research Model," *30th AIAA Applied Aerodynamics Conference*, 2012, AIAA 2012-3209.
- ¹¹Chen, H., Chen, S., and Matthaeus, W. H., "Recovery of the Navier-Stokes equations using a lattice-gas Boltzmann method," *Physical Review A*, Vol. 45, No. 8, 1992, pp. R5339-R5342.

- ¹²Qian, Y., d'Humieres, D., and Lallemand, P., "Lattice BGK Models for the Navier-Stokes Equation," *Europhysics Letters*, Vol. 17, 1992, pp. 479–484.
- ¹³Zhang, R., Shan, X., and Chen, H., "Efficient kinetic method for fluid simulation beyond the Navier-Stokes equation," *Physical Review E*, Vol. 74, Oct 2006, pp. 046703.
- ¹⁴Chen, H., Goldhirsch, I., and Orszag, S. A., "Discrete Rotational Symmetry, Moment Isotropy, and Higher Order Lattice Boltzmann Models," *Journal of Scientific Computing*, Vol. 34, No. 1, January 2008, pp. 87–112.
- ¹⁵Chen, H. and Shan, X., "Fundamental conditions for N-th-order accurate lattice Boltzmann models," *Physica D: Nonlinear Phenomena*, Vol. 237, No. 14–17, August 2008, pp. 2003–2008.
- ¹⁶Chen, H. and Teixeira, C., "H-theorem and origins of instability in thermal lattice Boltzmann models," *Computer Physics Communications*, Vol. 129, No. 1–3, 2000, pp. 21–31.
- ¹⁷Chen, H., Teixeira, C., and Molvig, K., "Digital Physics Approach to Computational Fluid Dynamics: Some Basic Theoretical Features," *International Journal of Modern Physics C*, Vol. 8, No. 4, 1997, pp. 675–684.
- ¹⁸Chen, H., Teixeira, C., and Molvig, K., "Realization of Fluid Boundary Conditions via Discrete Boltzmann Dynamics," *International Journal of Modern Physics C*, Vol. 09, No. 08, 1998, pp. 1281–1292.
- ¹⁹Chen, H., Kandasamy, S., Orszag, S., Shock, R., Succi, S., and Yakhot, V., "Extended Boltzmann Kinetic Equation for Turbulent Flows," *Science*, Vol. 301, No. 5633, 2003, pp. 633–636.
- ²⁰Shan, X., Yuan, X.-F., and Chen, H., "Kinetic theory representation of hydrodynamics: a way beyond the Navier Stokes equation," *Journal of Fluid Mechanics*, Vol. 550, 2006, pp. 413–441.
- ²¹Teixeira, C. M., "Incorporating Turbulence Models into the Lattice-Boltzmann Method," *International Journal of Modern Physics C*, Vol. 09, No. 08, 1998, pp. 1159–1175.
- ²²Brès, G., Wessels, M., and Noelting, S., "Tandem Cylinder Noise Predictions Using Lattice Boltzmann and Ffowcs-Williams-Hawking Methods," *16th AIAA/CEAS Aeroacoustics Conference*, 2010, AIAA 2010-3791.
- ²³Li, Y., Shock, R., Zhang, R., and Chen, H., "Numerical Study of Flow Past an Impulsively Started Cylinder by Lattice Boltzmann Method," *Journal of Fluid Mechanics*, Vol. 519, 2004, pp. 273–300.
- ²⁴Fares, E., Jelic, S., Kuthada, T., and Schroeck, D., "Lattice Boltzmann Thermal Flow Simulation and Measurements of a modified SAE Model with Heated Plug," *Proceedings of FEDSM2006*, 2006, FEDSM2006-98467.
- ²⁵Fares, E., "Unsteady Flow Simulation of the Ahmed Reference Body using a Lattice Boltzmann Approach," *Journal of Computers and Fluids*, Vol. 35, No. 8–9, 2006, pp. 940–950.
- ²⁶Casalino, D., Ribeiro, A. F. P., Fares, E., and Nölting, S., "Lattice Boltzmann Aeroacoustic Analysis of the LAGOON Landing-Gear Configuration," *AIAA Journal*, Vol. 52, No. 6, 2014, pp. 1232–1248.
- ²⁷Rivers, M. B. and Dittberner, A., "Experimental Investigations of the NASA Common Research Model in the NASA Langley National Transonic Facility and NASA Ames 11-Ft Transonic Wind Tunnel (Invited)," *49th AIAA Aerospace Sciences Meeting*, 2011, AIAA 2011-1126.
- ²⁸Rivers, M. B., Quest, J., and Rudnik, R., "Comparison of the NASA Common Research Model European Transonic Wind Tunnel Test Data to NASA Test Data (Invited)," *AIAA SciTech*, 2015, AIAA 2015-1093.
- ²⁹Makoto UENO, Takamasa KOHZAI, S. K., "JAXA Transonic Wind Tunnel Test of the NASA CRM (Volume 1)," Tech. Rep. ISSN 1349-1121, Institute of Aeronautical Technology, Wind Tunnel Technology Center, JAXA, 2014.
- ³⁰Diebold, J. M., Monastero, M. C., and Bragg, M. B., "Aerodynamics of a Swept Wing with Ice Accretion at Low Reynolds Number," *30th AIAA Applied Aerodynamics Conference*, 2012, AIAA 2012-2795.
- ³¹European Strategic Wind tunnels Improved Research Potential (ESWIRP), "The ESWIRP ETW TNA test results," <http://www.eswirp.eu/ETW-TNA-Dissemination.html>, retrived March 5th, 2015.
- ³²Keye, S. and Rudnik, R., "Validation of Wing Deformation Simulations for the NASA CRM Model using Fluid-Structure Interaction Computations," *53rd AIAA Aerospace Sciences Meeting*, 2015, AIAA 2015-0619.
- ³³Eberhardt, S., Benedict, K., Hedges, L., Robinson, A., and Tinoco, E. N., "Inclusion of Aeroelastic Twist into the CFD Analysis of the Twin-Engine NASA Common Research Model," *AIAA SciTech - 52nd Aerospace Sciences Meeting*, 2014, AIAA 2014-0251.